

Single-crystal diamond low-dissipation cavity optomechanics

Matthew Mitchell,^{1,2} Behzad Khanaliloo,^{1,2} David P. Lake,^{1,2}
Tamiko Masuda,¹ J.P. Hadden,¹ and Paul E. Barclay^{1,2,*}

¹*Department of Physics and Astronomy and Institute for Quantum Science and Technology,
University of Calgary, Calgary, AB, T2N 1N4, Canada*

²*National Institute for Nanotechnology, Edmonton, AB, T6G 2M9, Canada*

Single-crystal diamond cavity optomechanical devices are a promising example of a hybrid quantum system: by coupling mechanical resonances to both light and electron spins, they can enable new ways for photons to control solid state qubits. However, realizing cavity optomechanical devices from high quality diamond chips has been an outstanding challenge. Here we demonstrate single-crystal diamond cavity optomechanical devices that can enable photon-phonon-spin coupling. Cavity optomechanical coupling to 2 GHz frequency (f_m) mechanical resonances is observed. In room temperature ambient conditions, these resonances have a record combination of low dissipation (mechanical quality factor, $Q_m > 9000$) and high frequency, with $Q_m \cdot f_m \sim 1.9 \times 10^{13}$ sufficient for room temperature single phonon coherence. The system exhibits high optical quality factor ($Q_o > 10^4$) resonances at infrared and visible wavelengths, is nearly sideband resolved, and exhibits optomechanical cooperativity $C \sim 3$. The devices' potential for optomechanical control of diamond electron spins is demonstrated through radiation pressure excitation of mechanical self-oscillations whose 31 pm amplitude is predicted to provide 0.6 MHz coupling rates to diamond nitrogen vacancy center ground state transitions (6 Hz / phonon), and $\sim 10^5$ stronger coupling rates to excited state transitions.

1. INTRODUCTION

Diamond cavity optomechanical devices are an attractive platform for controlling interactions between light, vibrations, and electrons that underly future hybrid quantum technologies [1]. Their potential arises from diamond's exceptional mechanical and optical properties [2] combined with its ability to host color centers such as the nitrogen-vacancy (NV) whose electron spins are excellent qubits that can be manipulated by local mechanical strain fields [3–7]. Recently, piezoelectric actuation of bulk [3, 8] and nanomechanical [4–7, 9–11] diamond resonators has been used to demonstrate phononic spin control. Cavity optomechanics [12] harnesses optical forces in place of piezoelectric actuation, allowing coherent phonon state manipulation [13–15] of GHz frequency mechanical resonators with quantum limited sensitivity [16]. These phonons can be made resonant with NV center electron spin transitions that are central to proposals for spin–spin entanglement [17], spin–phonon state transfer [18–20], spin mediated mechanical normal mode cooling [17, 21, 22], and photon-phonon-spin coupling [23]. Additionally, the relatively small thermal occupancy and mechanical dissipation of GHz diamond devices, combined with diamond's ability to support strong optical fields due its large electronic bandgap, make them an ideal system for the cavity optomechanical backaction cooling and study of mechanical resonators in their quantum ground state [16].

Development of cavity optomechanical devices from single-crystal diamond has been limited due to challenges

associated with fabricating mechanically isolated structures from bulk diamond chips. While initial development of diamond optomechanical devices used nanocrystalline diamond [24], single crystal diamond material promises lower mechanical dissipation [25] and the ability to host highly coherent NV centers [26]. Here we report demonstration of a single-crystal diamond cavity optomechanical system for the first time. This system is based on a microdisk device geometry that has been used in a wide range of cavity optomechanics experiments implemented in more conventional semiconductor and dielectric materials [13, 15, 27, 28]. Microdisks are desirable owing to their simple geometry, strong optomechanical coupling between high frequency mechanical resonances and low loss optical modes, and intrinsic ability to simultaneously support optical modes over the entire transparency window of the device material [15].

The microdisk system studied here, an example of which is shown in Fig. 1(a), supports optical modes at visible and telecommunication wavelengths ($\omega/2\pi \sim 200 - 470$ THz) that interact via radiation pressure with GHz frequency mesoscopic mechanical resonances of the structure. We find that these resonances have a record combination of high ω_m and low mechanical dissipation ($\gamma_m = \omega_m/Q_m \sim 2\pi \times 0.2$ MHz) compared to other mechanical resonators operating in ambient temperature and pressure, and that their $Q_m \cdot f_m = 1.9 \times 10^{13}$ Hz product is sufficiently high to satisfy the minimum criteria for single phonon coherent behaviour [12]. The microdisk optical modes have low dissipation ($\gamma_o = \omega_o/Q_o \sim 2\pi \times 3$ GHz), and owing to the negligible nonlinear absorption in diamond at telecom optical frequencies, they can support intracavity photon number $N > 10^6$ without degrading Q_o . In combination, this allows realization of optomechanical cooperativity, $C = Ng_0^2/\gamma_o\gamma_m \sim 3$,

* pbarclay@ucalgary.ca

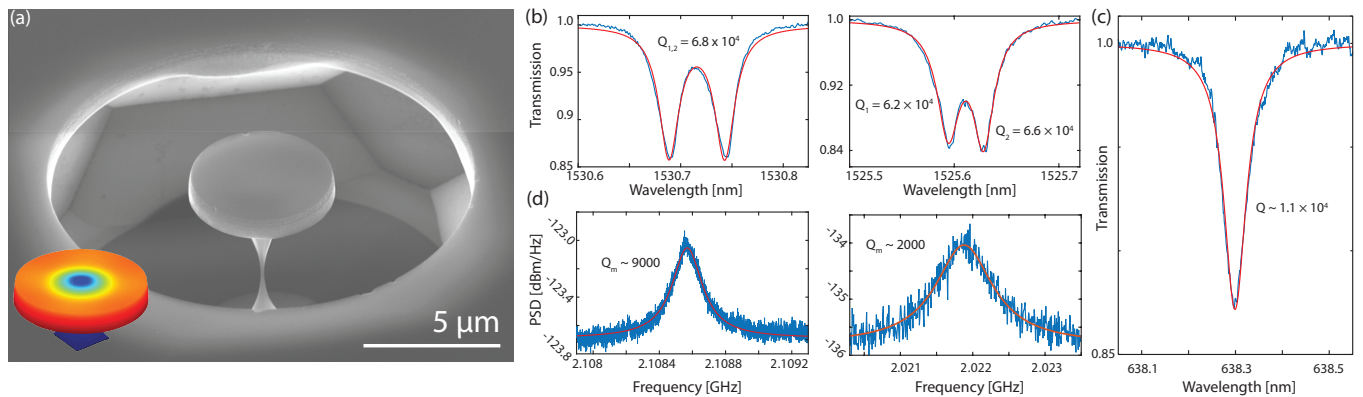


FIG. 1. Characterization of diamond microdisk optical and mechanical modes at low optical input power. (a) SEM image of a $5 \mu\text{m}$ diameter microdisk, with minimum pedestal width of 100 nm . Inset: Simulated displacement distribution of the RBM mechanical resonance of this device. (b) Highest Q_o TM-like optical modes of a $5 \mu\text{m}$ (left) and $5.5 \mu\text{m}$ (right) diameter microdisk, with intrinsic quality factors for each doublet resonances as labeled. (c) High- Q_o visible mode, with intrinsic quality factor as shown for a $6.2 \mu\text{m}$ diameter microdisk. (d) $S_P(f)$ produced by the thermal motion of the RBM of the microdisks in (b), showing that the larger diameter, larger pedestal waist microdisk has a lower Q_m .

large enough (> 1) for coherent photon-phonon coupling [13, 14], where $g_0 \sim 2\pi \times 26 \text{ kHz}$ is the single photon optomechanical coupling rate of the device and describes the expected shift in cavity optical frequency due to the mechanical zero point motion of the microdisk. These devices operate on the border of the sideband resolved regime ($\gamma_o \sim \omega_m$), enabling radiation pressure backaction excitation of mechanical self-oscillations with $\sim 31 \text{ pm}$ amplitude. The accompanying stress fields are strong enough to drive diamond color center spin transitions with a single phonon-spin coupling rate that is predicted to exceed that of previously studied MHz frequency nanomechanical structures [5–7], despite having orders of magnitude higher ω_m and smaller phonon amplitude, owing to the localized nature of the microdisk mechanical resonances. In addition, the ability of the microdisks to support optical modes at visible wavelengths is compatible with resonant coupling to NV center optical transitions [29], as well as operation in fluid environments of interest for sensing applications [27].

2. FABRICATION OF SINGLE-CRYSTAL DIAMOND MICRODISKS

There has been significant recent progress in fabrication of mechanically isolated single-crystal diamond devices, including demonstrations of suspended high- Q_m nanomechanical resonators [4, 25, 30–32] and high- Q_o micro- and nanocavities [33, 34]. These structures have been created using diamond membrane thinning [25, 30, 35], plasma angled-etching [33], and plasma undercutting [32, 34] fabrication techniques, with the latter two approaches allowing patterning of devices from bulk diamond chips. Here we use plasma undercutting to fabricate single crystal diamond cavity optomechanical devices [32, 34]. These

devices were fabricated from an optical grade, chemical vapor deposition (CVD) grown $\langle 100 \rangle$ -oriented SCD substrate supplied by Element Six. The polished substrates were first cleaned in boiling piranha, and coated with $\sim 400 \text{ nm}$ of plasma-enhanced chemical vapor deposition (PECVD) Si_3N_4 as a hard mask. To avoid charging effects during electron beam lithography (EBL), $\sim 5 \text{ nm}$ of Ti was deposited on the Si_3N_4 layer, before coating the sample with the ZEP 520A EBL resist. The developed pattern was transferred to the hard mask via inductively coupled reactive ion etching (ICPRIE) with $\text{C}_4\text{F}_8/\text{SF}_6$ chemistry. The remaining EBL resist was removed with a 6 minute deep-UV exposure ($5 \text{ mW}/\text{cm}^2$ at 254 nm) followed by a 2 minute soak in Remover PG, while the remaining Ti was removed by the subsequent etch steps. The anisotropic ICPRIE diamond etch was performed using O_2 , followed by deposition of $\sim 250 \text{ nm}$ of conformal PECVD Si_3N_4 as a sidewall protection layer. The bottom of the etch windows were then cleared of Si_3N_4 using a short ICPRIE $\text{C}_4\text{F}_8/\text{SF}_6$ etch. This was followed by a zero RF power O_2 RIE diamond undercut etch to partially release the devices. Lastly, the Si_3N_4 layer was removed using a wet-etch in 49% HF, and the devices were cleaned again in boiling piranha. The devices studied here have diameters of $5.0 \mu\text{m}$ to $6.0 \mu\text{m}$ and average thickness $\sim 940 \text{ nm}$. As evident from the image in Fig. 1(a), devices are fabricated with a process optimized to minimize the waist of the pedestal supporting the microdisk, reducing it to $< 100 \text{ nm}$, where the waist is defined as the smallest point of the pedestal. The microdisk thickness, which will be reduced in future work to enhance confinement, is determined by the interplay between the inward and upward etch rates of the quasi-isotropic undercut, together the initial anisotropic etch depth. The undercut time was chosen to optimize the pedestal waists of the $\sim 5 \mu\text{m}$ diameter disks studied

here. A longer undercut would allow the study of larger diameter microdisks (6 μm to 8 μm) present on the chip, which would in turn possess a smaller thickness than the structures studied here.

3. DEVICE CHARACTERIZATION

A. OPTICAL CHARACTERIZATION

The devices were characterized by monitoring the transmission of a dimpled optical fiber taper [36, 37] evanescently coupled to the microdisk and input with light from tunable diode lasers (New Focus Velocity) with wavelengths near 1530 nm or 637 nm. For the 1530 nm measurements, the output of the fiber taper was monitored by both low- and high-bandwidth photoreceivers (Newport 1621 and 1554-B, respectively), and a calibrated optical power meter (Newport 2936-R). Figure 1(b) shows typical $\bar{T}(\lambda_s)$ when the fiber taper is evanescently coupled to devices with diameters of 5.0 μm and 5.5 μm and the wavelength λ_s of the 1530 nm tunable laser is scanned across microdisk modes at λ_o . Here \bar{T} is the average transmission measured by the low-bandwidth photodetector over a timescale long compared to $1/f_m$. These measurements reveal resonant coupling to modes with loaded $Q_o \sim 5.8 \times 10^4 - 6.0 \times 10^4$ (intrinsic $Q_o^{(i)} = 6.1 \times 10^4 - 6.8 \times 10^4$), and a degree of doublet structure that depends on the internal backscattering of a given device. Maximizing Q_o , and thereby minimizing γ_o , is important for achieving the aforementioned regime allowing coherent photon-phonon coupling ($C > 1$).

The ability of these devices to support modes over a wide wavelength range is demonstrated in Fig. 1(c), where the 637 nm tunable laser was used to probe a mode with high- $Q_o > 1 \times 10^4$. This is promising for applications involving NV center optical transitions in this wavelength range [10]. These devices have a predicted radiation loss limited $Q_o > 10^7$ at both 1550 nm and 637 nm wavelengths; γ_o is currently limited by surface roughness and linear absorption. In previous work the microdisk pedestal size was observed to limit Q_o for insufficient relative undercut. In the devices studied here scattering due to the non-cylindrical pedestal shape is predicted to dominate the contribution to γ_o from the pedestal [34]. The lower Q_o observed at 637 nm can be attributed in part to sub-optimal fiber taper positioning [38] and an increased sensitivity to surface scattering [33].

B. CAVITY OPTOMECHANICAL COUPLING

To probe optomechanical coupling within the microdisks, time (t) dependent transmission fluctuations $\delta T(t, \lambda_s)$ of 1550 nm light were monitored using a real time spectrum analyzer (Tektronix RSA5106A). Excitations of the microdisk mechanical resonances modulate λ_o , resulting

in a dispersive optomechanical transduction of mechanical motion to an optical signal $P_o \delta T(t; \lambda_s)$ that can then be observed in the measured electronic power spectrum $S_P(f)$. Here P_o is the average power transmitted to the photoreceiver. Figure 1(d) shows typical spectra when λ_s is tuned near the point of maximum transduction of the modes in Fig. 1(b). Resonances near $f_m \sim 2.0 - 2.1$ GHz are observed, corresponding to optomechanical transduction of the thermomechanical motion of the fundamental radial breathing mode (RBM) of the microdisks. The predicted displacement of the RBM calculated using finite element simulations (COMSOL) is shown in the inset to Fig. 1(a). The simulated f_m of the RBM for varying microdisk diameter was found to be within 10% of observed values. These measurements were conducted at low input power $P_i \sim 50 \mu\text{W}$ to avoid optomechanical backaction effects discussed below. Here an erbium doped fiber amplifier (EDFA: Pritel LNHPFA-30) was used on the output side of the fiber taper to boost the optical signal prior to photodetection to a level just below the detector saturation power ($P_o \approx 0.7$ mW).

The microdisk pedestal can significantly affect the RBM properties, and minimizing its waist size is important in order to maximize Q_m and reach $C > 1$. In previously studied diamond microdisks with μm pedestal waists [34], transduction of mechanical modes was not observed. As shown in Fig. 1(a), the devices used here for cavity optomechanics have significantly smaller waists, e.g., the 5.0 μm diameter microdisks have waist < 100 nm. Figure 1(d) shows that when microdisk diameter, and as a result, pedestal waist are increased to 5.5 μm and 400 nm, respectively, Q_m is found to decrease from ~ 9000 to ~ 2000 . Mechanical resonances are not observed in devices with pedestal diameter > 500 nm. This indicates that Q_m for these devices is limited by clamping loss [28, 39]. The hourglass shape of the pedestals obtained for the $\langle 100 \rangle$ optical grade diamond samples used here limits the minimum size of the pedestal where it connects to the microdisk, and may result in increased dissipation. Given the crystal plane selective nature of the diamond undercut [34], fabricating microdisks from samples with alternate crystal orientation such as $\langle 111 \rangle$ may alleviate this limitation. Additionally, operation in vacuum, where viscous air damping can be avoided [40, 41], and at low temperature [25, 32] would allow a decrease in dissipation, as the total Q_m is given by $Q_m = (\sum_j 1/Q_m^j)^{-1}$, where the Q_m^j represent the quality factor due to each damping mechanism. Despite present limitations, the demonstrated devices have $Q_m \cdot f_m = 1.9 \times 10^{13}$ Hz, that is larger than all previously studied cavity optomechanical systems operating in ambient conditions [28, 39, 42]. A comparison of some of the highest $Q_m \cdot f_m$ products for optomechanical systems observed in ambient, cryogenic, and low pressure environments is shown in Supplement 1, Section 3. This figure of merit is critical for cavity optomechanical mass spectroscopy [27, 43, 44] and low phase noise oscillators [45]. Within the context of quantum optomechanics, this

product satisfies a key minimum requirement for room temperature studies of single phonon coherence by over an order of magnitude: $\omega_m/\gamma_m \gg n_{\text{th}}$, where n_{th} is the room temperature phonon population of the RBM, ensuring that thermal decoherence is slow compared to a mechanical oscillation [12]. By satisfying this condition, cooling to the quantum ground state from room temperature should also be possible [46].

To investigate the response of the cavity optomechanical transduction, S_P was monitored while λ_s was scanned across λ_o . Figure 2(a) shows the resulting measurement of $S_P(f, \lambda_s)$ for the microdisk in Fig. 1(a), clearly illustrating that optomechanical transduction is only observable when λ_s is tuned in the vicinity of λ_o . In this measurement the EDFA was connected to the input side of the fiber taper, resulting in maximum $N \sim 6.5 \times 10^5$ and $P_d \sim 1.5$ mW, where P_d is the optical power dropped into the microdisk mode. From the thermo-optic coefficient of diamond we estimate that the shift of 400 pm from the cold cavity λ_o , as seen in Figure 2(a), corresponds to a change in device temperature $\Delta T \sim 50$ K. COMSOL simulations that take into account the reduced thermal conductivity coefficient of the ~ 100 nm diameter pedestal compared to bulk [47] confirm that an absorbed power of $\sim 10\%$ of P_d reproduces the temperature shift observed here (see Supplement 1, Section 1). Although this temperature increase is not desirable for quantum optomechanics applications, it is considerably smaller than the expected increase for a similar Si device. Assuming a similar absorption rate and identical device geometry, a silicon device with a silicon or silicon dioxide pedestal would result in $\Delta T \sim 200$ K or 450 K, respectively, where a modified thermal conductivity also applies for the silicon in the pedestal [48]. It is expected that the rate of linear absorption observed here, which corresponds to $Q_o^{\text{abs}} = 6.2 \times 10^5$, can be reduced through improvements to processing, as diamond devices with $Q_o > 10^6$ have been reported elsewhere [49].

C. CAVITY OPTOMECHANICAL BACKACTION

The influence of cavity optomechanical backaction [12] on the dynamics of the mechanical resonator is analyzed in Figs. 2(b,c). Changes $\delta\gamma_m$ and $\delta\omega_m$ to γ_m and ω_m , respectively, were measured as a function of source-cavity detuning $\Delta = \omega_s - \omega_o$. Their strong dependence on Δ clearly indicates that the mechanical dynamics are affected by the intracavity field. We were prevented from measuring significant $\delta\gamma_m$ and $\delta\omega_m$ for red-detuned wavelengths ($\Delta < 0$) due to the thermal bistability present in our system for large P_d , as shown in Fig. 2(a). As such, this study concentrated on blue-detuned wavelengths ($\Delta > 0$), however implementation of cavity stabilization techniques [15] may allow this limitation to be overcome in the future, enabling more effective investigations of cavity sideband cooling [12, 16], and optome-

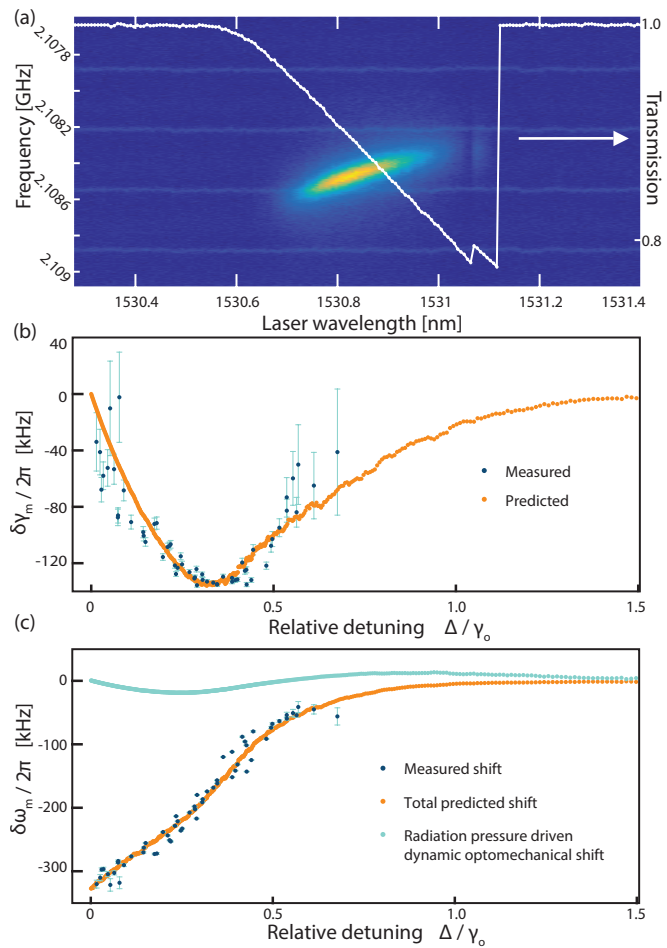


FIG. 2. Optomechanical backaction measurements. (a) $S_P(f, \lambda_s)$ and corresponding fiber transmission $T(\lambda)$ for P_i corresponding to maximum $N \sim 6.5 \times 10^5$ and $P_d \sim 1.5$ mW. The regularly spaced horizontal features are electronic noise from the apparatus. (b) Observed and predicted optomechanical linewidth narrowing of the RBM. The predicted $\delta\gamma_m$ depends on measured N and Δ for each point, as well as fitting parameter $g_0/2\pi = 26 \pm 2$ kHz. Error bars indicate 95% confidence interval for γ_m extracted from $S_P(f)$ at each data point. (c) Observed and predicted $\delta\omega_m$. Both the predicted shift due to optomechanical backaction for g_0 found from the fits in (b), and the predicted shift including an additional static thermal softening determined by a free fitting parameter, are shown.

chanically induced transparency [13–15]. Determining Δ for each data point in this analysis required accounting for the dependence of ω_o on N due to the thermo-optic effect. For a given operating ω_s , ω_o was predicted from N (see Supplement 1, Section 1), where $N(\omega_s)$ was determined from $\bar{T}(\omega_s)$, P_i , $Q_o^{(i)}$ and measurements of loss through the fiber taper and other elements of the apparatus.

To quantitatively investigate the role of radiation pressure on the mechanical resonance dynamics, the observed $\delta\gamma_m(\Delta)$ was fit to the expected cavity optomechanical

damping rate [12], with the single photon optomechanical coupling rate g_0 as the only free parameter. Using this method, the fit shown in Fig. 2(b) was obtained for $g_0/2\pi \sim 26$ kHz, with an associated 95% confidence interval of ± 2 kHz. Errors bars for each $\delta\gamma_m$ data point in Fig. 2(b) represent the 95% confidence interval of fits used to extract γ_m from S_P . The large uncertainty as well as the discrepancy between the measured and predicted values when $\Delta \sim 0$ or $\gg \gamma_o$ are due to the low signal to noise of S_P in these regions. This low signal to noise of S_P also prohibited measuring the optomechanical response for $\Delta \gg \gamma_o$. The fit value for g_0 has good agreement with g_0 predicted from COMSOL calculations that include both moving boundary (MB) and photoelastic (PE) contributions [50]. The predicted g_0 is dependent on the spatial overlap of the optical field and mechanical displacement profile, which varies for each optical mode. We find that the fit value of g_0 most closely agrees with the predicted coupling rate to the second order radial TM-like mode, with $g_{0_{PE}}/2\pi = 18$ to 24 kHz and $g_{0_{MB}}/2\pi = 16$ kHz. In comparison, $g_{0_{MB}}/2\pi = 17$ kHz (19 kHz) and $g_{0_{PE}}/2\pi = 29$ to 36 kHz (-24 to -26 kHz) for the fundamental TM (TE) mode of the microdisk. This is consistent with measurements of the mode polarization in the fiber taper that indicated that the microdisk mode studied here is TM polarized. Note that the stated uncertainty in the predicted $g_{0_{PE}}$ is due to variations in reported PE coefficients of single-crystal diamond [51].

Figure 2(c) shows a similar analysis of $\delta\omega_m(\Delta)$, indicating that ω_m is softened by over 300 kHz by the intracavity field. This shift is due to both optomechanical dynamical backaction and static thermal effects. For the operating regime and devices used here, dynamic thermal effects are expected to be below 5% of the optomechanical radiation pressure dynamical backaction effects, and can be neglected [42]. However, static thermal effects are significant. Heating of the microdisk for large P_d results in both thermal expansion and a change in Young's modulus, resulting in a shift to ω_m [52–54]. This effect is linear in P_d , assuming that Q_o is independent of power, i.e., nonlinear absorption is small. To compare the measured $\delta\omega_m(\Delta)$ with theory, we used a model that includes radiation pressure induced optomechanical dynamical backaction [12] and a static heating term linearly proportional to P_d :

$$\delta\omega_m(\Delta) = g_0^2 N \left(\frac{\Delta - \omega_m}{\gamma_o^2/4 + (\Delta - \omega_m)^2} + \frac{\Delta + \omega_m}{\gamma_o^2/4 + (\Delta + \omega_m)^2} \right) + \alpha P_d. \quad (1)$$

The resulting fit of (1) to the measured $\delta\omega_m$ is shown in Fig. 2(c) to have close agreement. Notably, this model reproduces the kink in $\delta\omega_m(\Delta)$ where the amplitude of the optomechanical contribution reaches a maximum and changes sign. This fit was obtained with g_0 fixed to the value extracted from the analysis of $\delta\gamma_m$ in Fig. 2(b), and with α as a fitting parameter.

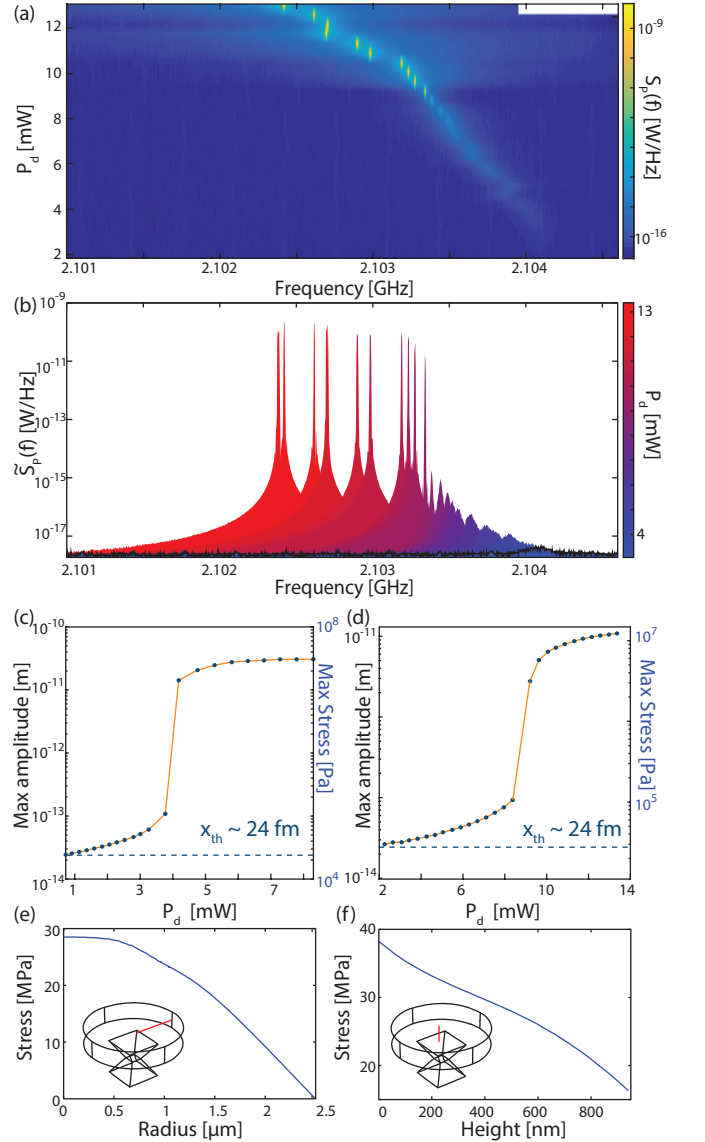


FIG. 3. Observation of microdisk self-oscillation. (a) $S_P(f; \lambda_{opt})$ as a function of dropped power. (b) Normalized cross-sections of (a), where $\tilde{S}_P(f)$ is given by $S_P(f; \lambda_{opt})$ normalized by the transduction gain so that the area under the curve represents the mechanical energy of the RBM. The black data is the thermal displacement spectra. (c, d) Maximum displacement and stress for 5 μ m diameter devices with (c) $Q_m \sim 9000$, $Q_o^{(t)} \sim 6 \times 10^4$, and (d) $Q_m \sim 8000$, $Q_o^{(t)} \sim 4 \times 10^4$. (e, f) Simulated stress along (e) radial and (f) vertical cuts in the microdisk, as indicated by the red lines in the insets, for the self-oscillating amplitude in (c).

At higher power the microdisk optomechanical dynamics can be dramatically modified. Figure 3 shows the behavior of the microdisk RBM when the input power to the fiber taper is increased sufficiently for P_d to reach 13 mW. This elevated power level corresponds to an intracavity photon number $N \sim 2.8 \times 10^6$, and an optomechanical cooperativity $C = Ng_0^2/\gamma_o\gamma_m = 2.7$ for the device shown

in Fig. 1(a). This C exceeds all previously reported values for devices operating in ambient conditions [14, 15]. For such large P_d , if the input λ_s is appropriately blue detuned from λ_o , it is possible for $\delta\gamma_m + \gamma_m \rightarrow 0$, resulting in self-oscillation of the microdisk RBM. Operation in this regime results in large dynamical strain within the microdisk, offering a potential path for achieving for large NV spin-phonon coupling.

We predict the strain achievable in our devices from measurements as follows. The microdisk mechanical response in the transition from thermal motion to self-oscillation is shown in Fig. 3(a), which displays $S_P(f; \lambda_{\text{opt}})$ for varying P_d , with λ_s tuned to the value λ_{opt} where $S_P(f_m)$ is maximum. As P_d is increased the mechanical resonance is observed to narrow and increase in amplitude, suggestive of the onset of self-oscillations, also referred to as phonon lasing. This is more clearly illustrated in Fig. 3(b), which shows the normalized spectrum $\tilde{S}_P(f)$ for varying P_d . Here $\tilde{S}_P(f)$ has been obtained by normalizing $S_P(f; \lambda_{\text{opt}})$ with the power dependent transduction gain, such that the area under $\tilde{S}_P(f)$ represents the mechanical energy of the RBM, i.e. \tilde{S}_P is constant with respect to P_i in absence of optomechanical backaction (see Supplement 1, Section 2). At low power, this mechanical energy is dominantly from the thermal bath, and is predicted from the equipartition theorem to correspond to oscillation amplitude $x_{\text{th}} \sim 24$ fm. Figures 3(c) and (d) show that for large P_d a maximum $x_{\text{om}} = 31$ pm is reached, likely limited by nonlinearity of the material. The corresponding predicted stress maximum associated with the self-oscillations, also shown in Figs. 3(c) and (d), is > 30 MPa. Stress values were determined from x_{om} and finite element simulations of the RBM displacement field shown in Fig. 1(a), and the maximum is predicted to occur at the center the microdisk top surface, as shown by the plots in Figs. 3(e,f). The corresponding maximum strain is $\approx 30 \times 10^{-6}$.

The self-oscillation threshold behaviour can be quantitatively analyzed by extracting the mechanical displacement amplitude x_{om} as a function of P_d from \tilde{S}_P . This is shown Figs. 3(c,d) for two similarly sized microdisks. In each case, a clear threshold is observed. Since these microdisks have different Q_m and Q_o (see Fig. 3 caption), their threshold power P_T differ. For devices close to the sideband resolved regime, the optimal detuning for self-oscillation to occur is $\Delta \sim \omega_m$, and P_T is given by [55]

$$P_T = \frac{m_{\text{eff}}\omega_o}{2g_{\text{om}}^2} \frac{\gamma_m\gamma_o^{(i)}}{\omega_m\gamma_o^{(t)}} (\gamma_o^{(t)}/2)^2 [(2\omega_m)^2 + (\gamma_o^{(t)}/2)^2] \quad (2)$$

where $g_{\text{om}} = g_0/x_{\text{zpm}}$ is the optomechanical coupling coefficient, and $\gamma_o^{(i)}$ and $\gamma_o^{(t)}$ are the intrinsic and fiber taper loaded optical decay rates, respectively. Here $x_{\text{zpm}} = \sqrt{\hbar/2m_{\text{eff}}\omega_m}$ is the mechanical zero point motion amplitude. For the devices studied here, $x_{\text{zpm}} \sim 0.32$ fm, as calculated from the RBM effective mass $m_{\text{eff}} \sim 40$ pg, predicted by the finite element simulated displacement field shown in Fig. 1(a) [12]. The observed $P_T = 3.5$ mW

and 8.5 mW, for the devices in Figs. 3(c) and 3(d) respectively, are above the predicted values of $760 \mu\text{W}$ and 3.0 mW obtained from (2) assuming g_0 is given by the fits in Fig. 2. This disagreement could be related to uncertainty in γ_o given that P_T scales to the fourth power of this quantity, interplay between doublets that is ignored by (2), and uncertainty in Δ inferred from the cavity response in the presence of thermo-optic dispersion.

4. DEVICE POTENTIAL FOR HYBRID SPIN-OPTOMECHANICS

The potential of these devices for hybrid spin-optomechanics applications can be measured by the predicted strain coupling rate g_e between a single phonon of the microdisk RBM and a single diamond NV center electron spin. The maximum zero point motion strain of the RBM is $\epsilon_{\text{zpm}} \approx 3 \times 10^{-10}$, and we estimate $g_e/2\pi = d\epsilon_{\text{zpm}} \approx 6$ Hz for a negatively charged NV^- center electron spin optimally located 50 nm below the top surface of the device in Fig. 3(c), exceeding the highest rate demonstrated to date [7]. Here $d \approx 10 - 20$ GHz is the strain susceptibility of the ground state spin [5, 6]. When the RBM is self-oscillating as in Fig. 3(c), the predicted coupling rate is $G/2\pi \approx 0.6$ MHz [5]. This is comparable to coupling rates achieved in piezoelectric actuated nanomechanical [5–7] and bulk devices [3, 8]. The longest room-temperature ground state spin decoherence time (T_2) observed to date in isotopically engineered single-crystal diamond is 1.8 ms [26], while typical T_2 values in nanostructures are on the order of 100 μs [5, 56]. Additionally, dynamical decoupling schemes can be utilized to extend this time, as $T_2 \sim 600$ ms has been observed at low temperature [57]. Photon–spin control should be possible provided $G/2\pi > T_2$, which is the case for these devices.

The GHz frequency of the RBM enables low room temperature phonon occupation, relevant for cooling to the quantum ground state from room temperature [16]. This also enables access to larger energy spin transitions [3, 8] than possible using previously demonstrated diamond nanomechanical resonators. This may be particularly important for future studies of phonon coupling to the NV^- center excited state manifold, which could achieve single phonon coupling rates close to a MHz due to the $\sim 10^5$ times larger strain susceptibility of the excited states [10, 22, 58, 59]. This is promising for implementing fully quantum photon-phonon-spin interfaces, and for proposals of spin-mediated cooling of nanomechanical resonators [17, 21, 22].

In the samples under study, we expect to find NVs optimally coupled to the RBM since the nitrogen concentration for this diamond sample (\sim ppm, corresponding to a number density of $1.76 \times 10^5 \mu\text{m}^{-3}$) results in high-concentration NV ensembles. However, future studies with higher purity samples may require NV implantation to optimally locate NVs ~ 50 nm below the device

surface. Additionally, due to minimal coupling of fluorescence from an NV centre located at the centre of the disk to the optical modes, free space collection would most likely be required. However, use of higher order radial breathing modes could allow for greater spatial overlap of the strain and electromagnetic field maxima [60], allowing for more efficient fiber based excitation and collection.

Future improvements of Q_o to values above 10^5 and approaching 10^6 should be possible [33, 34], enabling ultralow self-oscillation threshold [55] and operation deep in the sideband resolved regime required for optomechanical ground state cooling [16]. Operating in vacuum, at low temperature, and using devices fabricated from high-purity electronic grade diamond may allow further increases in Q_m [25], boosting the achievable photon-phonon cooperativity C and $Q_m \cdot f_m$ product. Similarly, reducing the microdisk diameter may increase C through enhanced g_0 , while also increasing ω_m . Simulations predict that diameters close to $3.5 \mu\text{m}$ are possible before radiation loss limits $Q_o < 10^5$; such devices would have $g_0/2\pi > 95 \text{ kHz}$ and $f_m \sim 3.4 \text{ GHz}$. Finally, using electronic grade diamond material and investigating processing techniques to reduce surface state absorption may decrease optical absorption and allow larger N before device heating becomes significant.

5. CONCLUSION

In conclusion, we have shown that cavity optomechanical devices can be realized from single-crystal diamond, with record high ambient condition optomechanical cooperativity, $C \sim 3$, and $Q_m \cdot f_m$ product of 1.9×10^{13} . These devices are a promising testbed for ambient condition coherent optomechanics experiments, e.g. ground state cooling [16], optomechanically induced transparency [13–15] and phonon mediated wavelength conversion [15, 61, 62], as well as studies in quantum information science [63], and hybrid quantum systems involving light, phonons, and diamond NV center spins [3, 5–7, 17, 21, 23]. We have also shown that the microdisks demonstrated here support high- Q_o optical modes at wavelengths near-resonant with the 637 nm optical transition of NV centers, further enhancing their potential for photon-phonon-spin coupling experiments.

We note that, in parallel to this work, Burek et al. have demonstrated cavity optomechanics in single-crystal diamond optomechanical crystals fabricated by a Faraday cage angled-etching technique [64].

We note that, in parallel to this work, Burek et al. have demonstrated cavity optomechanics in single-crystal diamond optomechanical crystals fabricated by a Faraday cage angled-etching technique [64].

Funding.

National Research Council Canada (NRC); Natural Sciences and Engineering Research Council of Canada (NSERC); National Institute for Nanotechnology (NINT), Canada Foundation for Innovation (CFI); Alberta Innovates–Technology Futures (AITF).

Acknowledgment.

The authors would like to thank A. C. Hryciw for his assistance with this project.

-
- [1] P. Treutlein, C. Genes, K. Hammerer, M. Poggio, and P. Rabl, in *Cavity Optomechanics* (Springer, 2014) pp. 327–351.
 - [2] I. Aharonovich, A. D. Greentree, and S. Prawer, *Nature Photon.* **5**, 397 (2011).
 - [3] E. R. MacQuarrie, T. A. Gosavi, N. R. Jungwirth, S. A. Bhawe, and G. D. Fuchs, *Phys. Rev. Lett.* **111**, 227602 (2013).
 - [4] J. Teissier, A. Barfuss, P. Appel, E. Neu, and P. Maletinsky, *Phys. Rev. Lett.* **113**, 020503 (2014).
 - [5] P. Ouartchaiyapong, K. W. Lee, B. A. Myers, and A. C. B. Jayich, *Nat. Commun.* **5**, 4429 (2014).
 - [6] A. Barfuss, J. Teissier, E. Neu, A. Nunnenkamp, and P. Maletinsky, *Nature Phys.* **11**, 820 (2015).
 - [7] S. Meesala, Y.-I. Sohn, H. A. Atikian, S. Kim, M. J. Burek, J. T. Choy, and M. Lončar, *Phys. Rev. Applied* **5**, 034010 (2016).
 - [8] E. R. MacQuarrie, T. A. Gosavi, A. M. Moehle, N. R. Jungwirth, S. A. Bhawe, and G. D. Fuchs, *Optica* **2**, 233 (2015).
 - [9] O. Arcizet, V. Jacques, A. Siria, P. Poncharal, P. Vincent, and S. Seidelin, *Nature Phys.* **7**, 879 (2011).
 - [10] D. A. Golter, T. Oo, M. Amezcua, K. A. Stewart, and H. Wang, *Phys. Rev. Lett.* **116**, 143602 (2016).
 - [11] K. W. Lee, D. Lee, P. Ouartchaiyapong, J. Minguzzi, J. R. Maze, and A. C. B. Jayich, arXiv:13603.07680 (2016).
 - [12] M. Aspelmeyer, T. J. Kippenberg, and F. Marquardt, *Rev. Mod. Phys.* **86**, 1391 (2014).
 - [13] S. Weis, R. Rivière, S. Deléglise, E. Gavartin, O. Arcizet, A. Schliesser, and T. J. Kippenberg, *Science* **330**, 1520 (2010).
 - [14] A. H. Safavi-Naeini, T. M. Alegre, J. Chan, M. Eichenfield, M. Winger, Q. Lin, J. T. Hill, D. Chang, and O. Painter, *Nature* **472**, 69 (2011).
 - [15] Y. Liu, M. Davanço, V. Aksyuk, and K. Srinivasan, *Phys. Rev. Lett.* **110**, 223603 (2013).
 - [16] J. Chan, T. P. M. Alegre, A. H. Safavi-Naeini, J. T. Hill, A. Krause, S. Groblacher, M. Aspelmeyer, and O. Painter, *Nature* **478**, 89 (2011).
 - [17] K. V. Kopeidis, S. D. Bennett, S. Portolan, M. D. Lukin, and P. Rabl, *Phys. Rev. B* **88**, 064105 (2013).
 - [18] P. Rabl, S. Kolkowitz, F. Koppens, J. Harris, P. Zoller, and M. Lukin, *Nature Phys.* **6**, 602 (2010).

- [19] K. Stannigel, P. Rabl, A. S. Sørensen, P. Zoller, and M. D. Lukin, *Phys. Rev. Lett.* **105**, 220501 (2010).
- [20] M. J. A. Schuetz, E. M. Kessler, G. Giedke, L. M. K. Vandersypen, M. D. Lukin, and J. I. Cirac, *Phys. Rev. X* **5**, 031031 (2015).
- [21] I. Wilson-Rae, P. Zoller, and A. Imamoglu, *Phys. Rev. Lett.* **92**, 075507 (2004).
- [22] E. MacQuarrie, M. Otten, S. Gray, and G. Fuchs, *arXiv:1605.07131* (2016).
- [23] T. Ramos, V. Sudhir, K. Stannigel, P. Zoller, and T. J. Kippenberg, *Phys. Rev. Lett.* **110**, 193602 (2013).
- [24] P. Rath, S. Khasminskaya, C. Nebel, C. Wild, and W. H. Pernice, *Nat. Commun.* **4**, 1690 (2013).
- [25] Y. Tao, J. M. Boss, B. A. Moores, and C. L. Degen, *Nat. Commun.* **5**, 3638 (2013).
- [26] G. Balasubramanian, P. Neumann, D. Twitchen, M. Markham, R. Kolesov, N. Mizuochi, J. Isoya, J. Achard, J. Beck, J. Tisler, V. Jacques, P. Hemmer, F. Jelezko, and F. Wrachtrup, *Nature Mater.* **8**, 383 (2009).
- [27] E. Gil-Santos, C. Baker, D. Nguyen, W. Hease, A. Lemaitre, S. Ducci, G. Leo, and I. Favero, *Nature Nanotech.* **10**, 810816 (2015).
- [28] X. Lu, J. Y. Lee, and Q. Lin, *Sci. Rep.* **5**, 17005 (2015).
- [29] A. Faraon, P. E. Barclay, C. Santori, K.-M. C. Fu, and R. G. Beausoleil, *Nature Photon.* **5**, 301 (2011).
- [30] P. Ovarthaiyapong, L. M. A. Pascal, B. A. Myers, P. Lauria, and A. C. Bleszynski Jayich, *Appl. Phys. Lett.* **101**, 163505 (2012).
- [31] M. J. Burek, N. P. de Leon, B. J. Shields, B. J. Hausmann, Y. Chu, Q. Quan, A. S. Zibrov, H. Park, M. D. Lukin, and M. Lončar, *Nano Lett.* **12**, 6084 (2012).
- [32] B. Khanaliloo, H. Jayakumar, A. C. Hryciw, D. P. Lake, H. Kaviani, and P. E. Barclay, *Phys. Rev. X* **5**, 041051 (2015).
- [33] M. J. Burek, Y. Chu, M. S. Z. Liddy, P. Patel, J. Rochman, S. Meesala, W. Hong, Q. Quan, M. D. Lukin, and M. Lončar, *Nat. Commun.* **5**, 5718 (2014).
- [34] B. Khanaliloo, M. Mitchell, A. C. Hryciw, and P. E. Barclay, *Nano Lett.* **15**, 5131 (2015).
- [35] P. Maletinsky, S. Hong, M. S. Grinolds, B. Hausmann, M. D. Lukin, R. L. Walsworth, M. Loncar, and A. Yacoby, *Nature Nanotech.* **7**, 320 (2012).
- [36] C. P. Michael, M. Borselli, T. J. Johnson, C. Chrystala, and O. Painter, *Opt. Express* **15**, 4745 (2007).
- [37] M. Mitchell, A. C. Hryciw, and P. E. Barclay, *Appl. Phys. Lett.* **104**, 141104 (2014).
- [38] M. Borselli, K. Srinivasan, P. E. Barclay, and O. Painter, *Appl. Phys. Lett.* **85**, 3693 (2004).
- [39] D. T. Nguyen, C. Baker, W. Hease, S. Sevil, P. Senellart, A. Lemaitre, S. Ducci, G. Leo, and I. Favero, *Appl. Phys. Lett.* **103**, 241112 (2013).
- [40] R. Rivière, *Cavity optomechanics with silica toroidal microresonators down to low phonon occupancy*, Ph.D. thesis, Ludwig-Maximilians-Universität München (2011).
- [41] X. Sun, X. Zhang, and H. X. Tang, *Appl. Phys. Lett.* **100**, 173116 (2012).
- [42] M. Eichenfield, J. Chan, R. Camacho, K. Vahala, and O. Painter, *Nature* **462**, 78 (2009).
- [43] K. Ekinci, Y. Yang, and M. Roukes, *J. Appl. Phys.* **95**, 2682 (2004).
- [44] W. Yu, W. C. Jiang, Q. Lin, and T. Lu, *arXiv:1504.03727* (2015).
- [45] C. T.-C. Nguyen, *IEEE Transactions on Ultrasonics, Ferroelectrics and Frequency Control* **54**, 251 (2007).
- [46] R. A. Norte, J. P. Moura, and S. Gröblacher, *Phys. Rev. Lett.* **116**, 147202 (2016).
- [47] W. Li, N. Mingo, L. Lindsay, D. A. Broido, D. A. Stewart, and N. A. Katcho, *Phys. Rev. B* **85**, 195436 (2012).
- [48] D. Li, Y. Wu, P. Kim, L. Shi, P. Yang, and A. Majumdar, *Appl. Phys. Lett.* **83**, 2934 (2003).
- [49] B. J. Hausmann, I. Bulu, V. Venkataraman, P. Deotare, and M. Lončar, *Nature Photon.* **8**, 369 (2014).
- [50] J. Chan, A. Safavi-Naeini, J. Hill, S. Meenehan, and O. Painter, *Appl. Phys. Lett.* **101**, 081115 (2012).
- [51] L. S. Hounsborne, R. Jones, M. J. Shaw, and P. R. Briddon, *Phys. Status Solidi A* **203**, 3088 (2006).
- [52] D. T. Nguyen, W. Hease, C. Baker, E. Gil-Santos, P. Senellart, A. Lematre, S. Ducci, G. Leo, and I. Favero, *New J. Phys.* **17**, 023016 (2015).
- [53] J. R. Clark, W.-T. Hsu, M. A. Abdelmoneum, and C. T.-C. Nguyen, *Jour. of Micro. Sys.* **14**, 1298 (2005).
- [54] R. Yang, Z. Wang, J. Lee, K. Ladhane, D. J. Young, and P. X. L. Feng, in *Frequency Control Symposium (FCS), 2014 IEEE International* (2014) pp. 1–3.
- [55] W. C. Jiang, X. Lu, J. Zhang, and Q. Lin, *Opt. Express* **20**, 15991 (2012).
- [56] J. Hodges, L. Li, M. Lu, E. H. Chen, M. Trusheim, S. Allegri, X. Yao, O. Gaathon, H. Bakhru, and D. Englund, *New J. Phys.* **14**, 093004 (2012).
- [57] N. Bar-Gill, L. Pham, A. Jarmola, D. Budker, and R. Walsworth, *Nat. Commun.* **4**, 1743 (2013).
- [58] G. Davies and M. F. Hamer, *Proc. R. Soc. Lond. A* **348**, 285 (1976).
- [59] A. Batalov, V. Jacques, F. Kaiser, P. Siyushev, P. Neumann, L. J. Rogers, R. L. McMurtrie, N. B. Manson, F. Jelezko, and J. Wrachtrup, *Phys. Rev. Lett.* **102**, 195506 (2009).
- [60] C. Baker, W. Hease, D.-T. Nguyen, A. Andronico, S. Ducci, G. Leo, and I. Favero, *Opt. Express* **22**, 14072 (2014).
- [61] C. Dong, V. Fiore, M. C. Kuzyk, and H. Wang, *Science* **338**, 1609 (2012).
- [62] J. T. Hill, A. H. Safavi-Naeini, J. Chan, and O. Painter, *Nat. Commun.* **3**, 1196 (2012).
- [63] K. Stannigel, P. Komar, S. J. M. Habraken, S. D. Bennett, M. D. Lukin, P. Zoller, and P. Rabl, *Phys. Rev. Lett.* **109**, 013603 (2012).
- [64] M. J. Burek, J. D. Cohen, S. M. Meenehan, T. Ruelle, S. Meesala, J. Rochman, H. A. Atikian, M. Markham, D. J. Twitchen, M. D. Lukin, O. Painter, and M. Lončar, *arXiv:1512.04166* (2015).

SINGLE-CRYSTAL DIAMOND LOW-DISSIPATION CAVITY OPTOMECHANICS: SUPPLEMENTARY MATERIAL

1. THERMAL SHIFT AND BISTABILITY

Here we outline the process for extracting the power dependent detuning, Δ . This process follows Carmon et al. [S1], beginning with the expression for the shifted cavity resonance wavelength as a function of temperature, in thermal equilibrium

$$\lambda'_o(\Delta T) = \lambda_o + \Delta\lambda_o, \quad (\text{S1})$$

$$= \lambda_o \left[1 + \left(\eta_\epsilon \epsilon + \eta_T \frac{1}{n} \frac{dn}{dT} \right) \Delta T \right], \quad (\text{S2})$$

$$= \lambda_o [1 + a\Delta T]. \quad (\text{S3})$$

This expression is obtained by considering thermal expansion of the cavity, determined by the thermal expansion coefficient ϵ , and the thermo-optic effect, which shifts the refractive index n with temperature T . Here η_T and η_ϵ are geometric factors accounting for the optical mode overlap with the changing n and volume, respectively. Lumped constant a describes the net thermo-optic dispersion of the cavity mode. Using the room temperature single-crystal diamond values of $\epsilon \sim 1 \times 10^{-6}$ and $dn/dT \sim 1 \times 10^{-5}$ we can estimate the change in temperature of the cavity as

$$\Delta T = \left[\frac{\lambda'_o(\Delta T)}{\lambda_o} - 1 \right] \cdot \frac{1}{a}. \quad (\text{S4})$$

The shift of $\Delta\lambda_o \sim 400$ pm, as seen in Fig. 2(a) of the main text, corresponds to a change in device temperature $\Delta T \sim 50$ K. In this device the diamond forming the ~ 100 nm diameter pedestal has a significantly smaller thermal conductivity than that of bulk diamond ($K \sim 1500 \text{ Wm}^{-1}\text{K}^{-1}$), reaching values $< 100 \text{ Wm}^{-1}\text{K}^{-1}$ for nanowires < 100 nm in diameter [S2]. In order to confirm that the cavity temperature shift predicted by (S4) was reasonable for our system we performed finite element COMSOL simulations to estimate ΔT , including the modified thermal conductivity for the pedestal, as shown in Fig. S1 for varying pedestal widths. Fig. S1 indicates that for a pedestal width of ~ 100 nm, and corresponding diamond thermal conductivity of $\sim 300 \text{ Wm}^{-1}\text{K}^{-1}$ a shift of 50 K is expected when $P_{\text{abs}} \sim 170 \mu\text{W}$, where P_{abs} is the total power absorbed by the cavity. This corresponds to an optical absorption rate, $\gamma_{\text{abs}} \times 2\pi \sim 312$ MHz, which is $\sim 10\%$ of the total cavity decay rate, γ_{tot} . A linear relationship between ΔT and P_{abs} is observed for the pedestal thicknesses studied here.

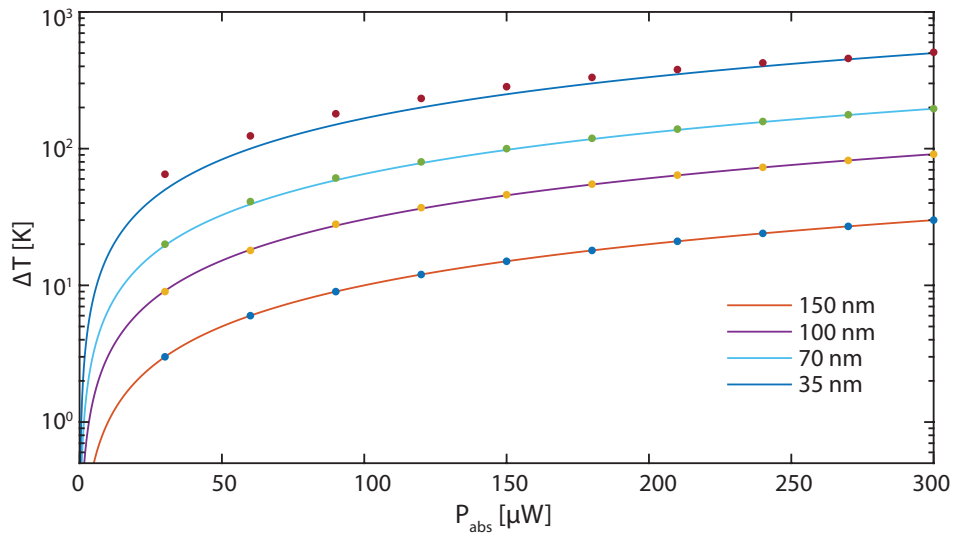


FIG. S1. Simulated change in temperature, ΔT of a $\sim 5 \mu\text{m}$ diameter microdisk as a function of absorbed power, P_{abs} for varying pedestal widths. Here the total heat flow to the device is given by P_{abs}/V , where V is the volume defined by the outer edge of the microdisk, with $V \sim 2 \mu\text{m}^3$. Each line represents a linear line of best fit to ΔT as a function of P_{abs} .

To convert (S3) to a form that depends on the experimentally measured, normalized cavity transmission \bar{T} , we treat the microdisk as being in thermal equilibrium with its environment such that

$$\dot{q}_{\text{in}} = \frac{\gamma_{\text{abs}}}{\gamma_{\text{tot}}} P_d, \quad (\text{S5})$$

where \dot{q}_{in} , and P_d are the heat flow and power dropped into the cavity, respectively. Furthermore, we assume that

$$\dot{q}_{\text{out}} = K \Delta T, \quad (\text{S6})$$

where K is the thermal conductivity between the cavity mode volume and the surrounding [S1]. In thermal equilibrium the heat flow into the cavity will be equal to the heat flow out of the cavity, which allows us to write the equilibrium temperature as

$$\Delta T = \frac{\gamma_{\text{abs}}}{\gamma_{\text{tot}}} \frac{P_d}{K}. \quad (\text{S7})$$

Next we observe that since $P_d = (1 - \bar{T})P_i$ where P_i is the fiber taper waveguide input power, we can write

$$\Delta T = \frac{\gamma_{\text{abs}}}{\gamma_{\text{tot}}} \frac{(1 - \bar{T})P_i}{K}, \quad (\text{S8})$$

and the expected cavity mode shift in terms of the resonance contrast

$$\lambda'_o(\Delta T) = \lambda_o [1 + a \Delta T], \quad (\text{S9})$$

$$= \lambda_o \left[1 + \left(\frac{a}{K} \frac{\gamma_{\text{abs}}}{\gamma_{\text{tot}}} P_i \right) (1 - \bar{T}) \right], \quad (\text{S10})$$

$$= \lambda_o [1 + d(1 - \bar{T})]. \quad (\text{S11})$$

This gives the laser-cavity wavelength detuning, Δ_λ as

$$\Delta_\lambda = \lambda_s - \lambda'_o, \quad (\text{S12})$$

$$= \lambda_s - \lambda_o - d(1 - \bar{T}). \quad (\text{S13})$$

where $d = \frac{a}{K} \frac{\gamma_{\text{abs}}}{\gamma_{\text{tot}}} P_i$ is used as a free parameter in fitting our cavity transmission profile. The laser detuning Δ can then be calculated for any bistable lineshape.

2. SELF OSCILLATIONS AND DISPLACEMENT AMPLITUDE

In the weak damping regime ($\gamma_m \ll \omega_m$) the oscillation amplitude of a thermally driven harmonic oscillator is given by the equipartition theorem [S3] as

$$x_{\text{th}} = \sqrt{\frac{k_B T}{m_{\text{eff}} \omega_m^2}}, \quad (\text{S14})$$

where k_B is the Boltzmann constant, $T = 295$ K is the bath temperature, and $m_{\text{eff}} = 40$ pg and $\omega_m/2\pi \sim 2$ GHz are the effective mass and mechanical frequency of the radial breathing mode studied here, respectively. This results in $x_{\text{th}} = 24$ fm and a zero point fluctuation motion, $x_{\text{zpm}} = 0.32$ fm.

While $S_P(f) \propto \langle x^2 \rangle$, where $\langle x^2 \rangle$ is the variance of the mechanical displacement, one must be more careful when calculating the mechanical energy. Strictly speaking $\langle x^2 \rangle$ is related to the single sided displacement spectral density $S_{xx}(\omega)$ by

$$\langle x^2 \rangle = \int_0^\infty S_{xx}(\omega) \frac{d\omega}{2\pi}. \quad (\text{S15})$$

This can be connected to the measured cavity transmission noise spectrum $S_P(\omega)$ through a cavity transfer function $H(\omega, \Delta)$, P_i , and g_{om} [S4]

$$S_P(\omega) = g_{\text{om}}^2 P_i^2 S_{xx}(\omega) H(\omega, \Delta). \quad (\text{S16})$$

In this experiment we measure $S_P(\omega)$, and can compute the area under the curve, A , given by $A = \int_0^\infty S_P(\omega) \frac{d\omega}{2\pi}$. If we change P_i from P_{i_1} to P_{i_2} , keep Δ constant, and ignore the small ($\sim 0.02\%$) changes in ω_m , such that $H(\omega, \Delta; P_{i_1}) = H(\omega, \Delta; P_{i_2})$, we can show that the ratio of the area under the curve corresponding to P_{i_1} and P_{i_2} given by A_1 and A_2 , respectively, is

$$\frac{A_1}{A_2} = \frac{P_{i_1}^2 \langle x_1^2 \rangle}{P_{i_2}^2 \langle x_2^2 \rangle}. \quad (\text{S17})$$

We can then calibrate high P_i measurements to the thermal case, where P_i is small enough for optomechanical backaction effects to be ignored. The displacement amplitude, x_{om} , of the RBM in the self-oscillation regime can then be calculated as

$$x_{\text{om}} = x_{\text{th}} \sqrt{\frac{A_{\text{om}} P_T^2}{A_{\text{th}} P_{\text{om}}^2}}, \quad (\text{S18})$$

where A_{om} and A_{th} are the area under the curve in the driven ($P_i = P_{\text{om}}$) and thermal ($P_i = P_T$) states, respectively. Similarly, for the purpose of comparing mechanical spectra it is useful to calculate the normalized cavity transmission noise spectrum \tilde{S}_P , given by

$$\tilde{S}_P(\omega; P_i, \Delta) = S_P(\omega; P_i) \frac{P_i^2}{P_T^2} \Big|_{\Delta}. \quad (\text{S19})$$

The maximum oscillation amplitude x_{om} is shown as a function of dropped optical power in Fig. 3(a), where the absolute maximum oscillation amplitude was found to be ~ 31 pm ($\sim x_{\text{th}} \cdot 10^3$). Using finite element COMSOL simulations and by assuming that diamond behaves as a linear elastic material in the self oscillation regime, these amplitudes correspond to stress on the order of tens of MPa at the center of the microdisk.

3. COMPARISON OF $Q_m \cdot f_m$ PRODUCT

The device studied here demonstrates the largest $Q_m \cdot f_m$ product of an optomechanical device measured in ambient conditions to date. Figure S2 compares this value with a survey of some of the largest $Q_m \cdot f_m$ products observed in cavity optomechanical systems in ambient, cryogenic, and low pressure conditions. Note that higher $Q_m \cdot f_m$ products have been demonstrated compared to this work, but required either vacuum or low-temperature environments.

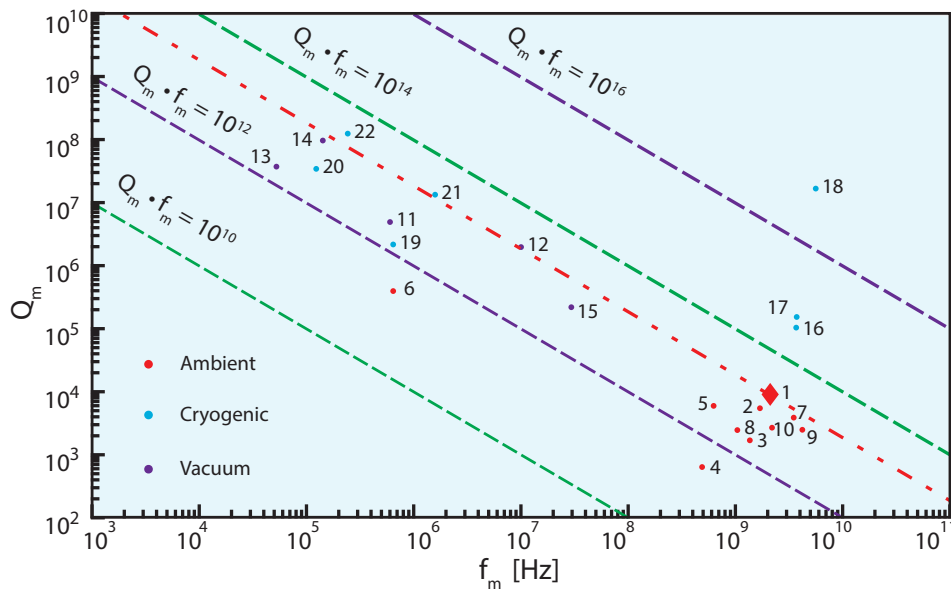


FIG. S2. Comparison of high $Q_m \cdot f_m$ products for a variety of optomechanical systems, as listed in Table S1.

TABLE S1. Survey of highest $Q_m \cdot f_m$ products observed in cavity optomechanical systems to date, corresponding to those shown in Fig. S2.

No.	Author/Reference	Material	Structure
1	Mitchell et al. (This Work)	Diamond	Microdisk
2	Lu et al. [S5]	SiC	Microdisk
3	Nguyen et al. [S6]	GaAs	Microdisk
4	Mitchell et al. [S7]	GaP	Microdisk
5	Liu et al. [S8]	Si ₃ N ₄	Microdisk
6	Fong et al. [S9]	Si ₃ N ₄	Beam & Waveguide
7	Grutter et al. [S10]	Si ₃ N ₄	Optomechanical Crystal
8	Xiong et al. [S11]	AlN	Suspended Ring Resonator
9	Bochmann et al. [S12]	AlN	Optomechanical Crystal
10	Eichenfield et al. [S13]	Si	Optomechanical Crystal
11	Bui et al. [S14]	Si ₃ N ₄	Membrane Photonic Crystal + Fabry P�erot Cavity
12	Wilson et al. [S15]	Si ₃ N ₄	Membrane + Fabry P�erot Cavity
13	Reinhardt et al. [S16]	Si ₃ N ₄	Membrane + Fabry P�erot Cavity
14	Norte et al. [S17]	Si ₃ N ₄	Membrane Photonic Crystal + Fabry P�erot Cavity
15	Zhang et al. [S18]	Si ₃ N ₄	Tuning Fork + Microdisk
16	Chan et al. [S19]	Si	Optomechanical Crystal + Phononic Shield
17	Krause et al. [S20]	Si	Optomechanical Crystal + Phononic Shield
18	Meenehan et al. [S21]	Si	Optomechanical Crystal + Phononic Shield
19	Fong et al. [S9]	Si ₃ N ₄	Beam + On-chip Interferometer
20	Yuan et al. [S22]	Si ₃ N ₄	Membrane + Superconducting Microwave Cavity
21	Purdy et al. [S23]	Si ₃ N ₄	Membrane + Fabry P�erot Cavity
22	Yuan et al. [S24]	Si ₃ N ₄	Membrane + Superconducting Microwave Cavity

- [S1] T. Carmon, L. Yang, and K. J. Vahala, *Opt. Express* **12**, 4742 (2004).
- [S2] W. Li, N. Mingo, L. Lindsay, D. A. Broido, D. A. Stewart, and N. A. Katcho, *Phys. Rev. B* **85**, 195436 (2012).
- [S3] M. Aspelmeyer, T. J. Kippenberg, and F. Marquardt, *Rev. Mod. Phys.* **86**, 1391 (2014).
- [S4] Q. Lin, J. Rosenberg, D. Chang, R. Camacho, M. Eichenfield, K. J. Vahala, and O. Painter, *Nature Photon.* **4**, 236 (2010).
- [S5] X. Lu, J. Y. Lee, and Q. Lin, *Sci. Rep.* **5**, 17005 (2015).
- [S6] D. T. Nguyen, C. Baker, W. Hease, S. Sejlil, P. Senellart, A. Lemaitre, S. Ducci, G. Leo, and I. Favero, *Appl. Phys. Lett.* **103**, 241112 (2013).
- [S7] M. Mitchell, A. C. Hryciw, and P. E. Barclay, *Appl. Phys. Lett.* **104**, 141104 (2014).
- [S8] Y. Liu, M. Davanço, V. Aksyuk, and K. Srinivasan, *Phys. Rev. Lett.* **110**, 223603 (2013).
- [S9] K. Y. Fong, W. H. P. Pernice, and H. X. Tang, *Phys. Rev. B* **85**, 161410 (2012).
- [S10] K. E. Grutter, M. I. Davanço, and K. Srinivasan, *Optica* **2**, 994 (2015).
- [S11] C. Xiong, X. Sun, K. Y. Fong, and H. X. Tang, *Appl. Phys. Lett.* **100**, 171111 (2012).
- [S12] J. Bochmann, A. Vainsencher, D. D. Awschalom, and A. N. Cleland, *Nature Phys.* **9**, 712716 (2013).
- [S13] M. Eichenfield, J. Chan, R. Camacho, K. Vahala, and O. Painter, *Nature* **462**, 78 (2009).
- [S14] C. H. Bui, J. Zheng, S. W. Hoch, L. Y. T. Lee, J. G. E. Harris, and C. Wei Wong, *Appl. Phys. Lett.* **100**, 021110 (2012).
- [S15] D. J. Wilson, C. A. Regal, S. B. Papp, and H. J. Kimble, *Phys. Rev. Lett.* **103**, 207204 (2009).
- [S16] C. Reinhardt, T. M uller, A. Bourassa, and J. C. Sankey, arXiv:1511.01769 (2016).
- [S17] R. A. Norte, J. P. Moura, and S. Gr oblacher, *Phys. Rev. Lett.* **116**, 147202 (2016).
- [S18] R. Zhang, C. Ti, M. I. Davano, Y. Ren, V. Aksyuk, Y. Liu, and K. Srinivasan, *Appl. Phys. Lett.* **107**, 131110 (2015).
- [S19] J. Chan, T. P. M. Alegre, A. H. Safavi-Naeini, J. T. Hill, A. Krause, S. Groblacher, M. Aspelmeyer, and O. Painter, *Nature* **478**, 89 (2011).
- [S20] A. G. Krause, J. T. Hill, M. Ludwig, A. H. Safavi-Naeini, J. Chan, F. Marquardt, and O. Painter, *Phys. Rev. Lett.* **115**, 233601 (2015).
- [S21] S. M. Meenehan, J. D. Cohen, G. S. MacCabe, F. Marsili, M. D. Shaw, and O. Painter, *Phys. Rev. X* **5**, 041002 (2015).
- [S22] M. Yuan, V. Singh, Y. M. Blanter, and G. A. Steele, *Nat. Commun.* **6** (2015).
- [S23] T. P. Purdy, R. W. Peterson, P.-L. Yu, and C. A. Regal, *New J. Phys.* **14**, 115021 (2012).
- [S24] M. Yuan, M. A. Cohen, and G. A. Steele, *Appl. Phys. Lett.* **107**, 263501 (2015).